Direct probing of atomically dispersed Ru species over multi-edged TiO2 for highly efficient photocatalytic hydrogen evolution

Zhang, Huabin; Zuo, Shouwei; Qiu, Mei; Wang, Sibo; Zhang, Yongfan; Zhang, Jing; Lou, David Xiong Wen

CHEMISTRY

Direct probing of atomically dispersed Ru species over multi-edged TiO₂ for highly efficient photocatalytic hydrogen evolution

Huabin Zhang[1], Shouwei Zuo[2], Mei Qiu[3], Sibo Wang[1], Yongfan Zhang[3], Jing Zhang[2], Xiong Wen (David) Lou[1]*

A cocatalyst is necessary for boosting the electron-hole separation efficiency and accelerating the reaction kinetics of semiconductors. As a result, it is of critical importance to in situ track the structural evolution of the cocatalyst during the photocatalytic process, but it remains very challenging. Here, atomically dispersed Ru atoms are decorated over multi-edged TiO₂ spheres for photocatalytic hydrogen evolution. Experimental results not only demonstrate that the photogenerated electrons can be effectively transferred to the isolated Ru atoms for hydrogen evolution but also imply that the TiO₂ architecture with multi-edges might facilitate the charge separation and transport. The change in valence and the evolution of electronic structure of Ru sites are well probed during the photocatalytic process. Specifically, the optimized catalyst produces the hydrogen evolution rate of 7.2 mmol g⁻¹ hour⁻¹, which is much higher than that of Pt-based cocatalyst systems and among the highest reported values.

INTRODUCTION

Photocatalytic water splitting using semiconductor photocatalysts has been considered as a sustainable manner to produce clean hydrogen (H₂) fuel (*1, 2*). Cocatalysts are usually deposited onto the surface of photocatalysts for retarding the recombination of charge carriers and enhancing the surface reaction (*3–6*). Pt often exhibits the best performance among various cocatalysts. However, the practical applications of Pt-based cocatalysts are heavily limited by their scarcity and high cost. Therefore, the development of highly active and cost-efficient alternatives to Pt is urgently needed. As a cheaper alternative to Pt, Ru has a similar bond strength with hydrogen (ca. 65 kcal mol⁻¹), but the activities of Ru-based cocatalysts are still far from satisfactory (*7, 8*). Since only surface atoms are involved in the reaction as active sites, there should be great room for boosting the catalytic efficiency (*9*).

Reducing the size of the cocatalyst to isolated atoms represents the downsizing limit for the maximized atom utilization efficiency. Moreover, uniformly distributed isolated active sites provide us an elegant platform for exploring precise structure-performance relationships at the atomic/molecular levels (*10*). The electronic structure variation of the cocatalysts and their interactions with light absorbers are of vital importance for understanding the mechanism during photocatalysis (*11*). Single-atom catalysts, with nearly identical catalytically active sites, offer us the opportunity to monitor the structural evolution during the reaction process (*12*). However, deterministic identification of the local atomic configuration and the corresponding dynamic process is still very challenging.

Here, we decorated isolated Ru atoms (the cocatalyst) over the multi-edged TiO₂ sphere (denoted as ME-TiO₂@Ru) for efficient photocatalytic H₂ evolution. ME-TiO₂ with a sharp boundary speeds up electron transfer along with the highly oriented crystals to the atomically dispersed Ru cocatalyst, which greatly improves the efficiency of H₂ evolution. In particular, the in situ x-ray absorption fine structure (XAFS) technique has been applied for probing the dynamic evolution of the isolated sites during the catalytic process. Upon light irradiation, the Ru species gradually undergo valence and configuration evolution, thereby photo-splitting water into solar fuels in a dynamic manner.

RESULTS

Synthesis and structural characterization

The multistep synthetic process for the ME-TiO₂@Ru hierarchical structure is depicted in Fig. 1. Multi-edged protonated titanate (ME-PT) hierarchical spheres are synthesized as the starting template (see the Supplementary Materials and fig. S1A) (*13*). Field-emission scanning electron microscopy (FESEM) image reveals that the obtained sample has open-up architecture with a nanosheet surface structure (fig. S2A). Transmission electron microscopy (TEM) observation around the edge of the hierarchical spheres reveals the almost transparent layers, suggesting that the nanosheets are ultrathin (fig. S2, B and C). Subsequently, the as-prepared ME-PT is mixed with RuCl₃ in ethanol solution for 2 hours for loading the Ru species over the surface of ME-PT. The zeta potential investigation confirms that ME-PT is negatively charged in ethanol solution and the Ru species (in ethanol solution) have the opposite interfacial charges. They would be assembled spontaneously through the electrostatic interaction, resulting in the adsorption of Ru on the surface of ME-PT (denoted as ME-PT@Ru) (fig. S1B) (*9*). FESEM and TEM investigations confirm that the original architecture of ME-PT is well maintained after Ru decoration (Fig. 2, A to D). The as-prepared ME-PT and ME-PT@Ru are converted into ME-TiO₂ and ME-TiO₂@Ru, respectively, through the pyrolysis in air (figs. S1C and S2, D to F). The conversion process is also monitored by thermogravimetric analysis. An obvious weight loss is observed between 200° and 450°C, corresponding to the removal of the organic component and the transformation of ME-PT@Ru into ME-TiO₂@Ru (fig. S3).

FESEM observation over ME-TiO₂@Ru shows the well-retained architecture with slight shrinkage (Fig. 2, E and F). TEM and

¹School of Chemical and Biomedical Engineering, Nanyang Technological University, 62 Nanyang Drive, Singapore 637459, Singapore. ²Beijing Synchrotron Radiation Facility, Institute of High Energy Physics, Chinese Academy of Sciences, Beijing 100049, China. ³College of Chemistry, Fuzhou University, Fuzhou 350108, China.
*Corresponding author. Email: xwlou@ntu.edu.sg

high-resolution TEM (HRTEM) investigations not only confirm the sheet-like microstructure with multi-edges but also verify the generation of anatase TiO_2 crystallites with presumably exposed (101) facets (Fig. 2, G to K). No apparent Ru nanoparticles or clusters are observed, indicating that no aggregation of Ru species has occurred. X-ray diffraction (XRD) pattern of ME-TiO_2@Ru only shows identical diffraction peaks of anatase TiO_2, which agrees with the lattice fringes in HRTEM images (fig. S1D) (*14*). The high-angle annular dark-field scanning TEM (HAADF-STEM) image, energy-dispersive x-ray spectroscopy spectra, and elemental mapping images indicate that the Ru species is distributed uniformly over the entire ME-TiO_2@Ru sphere (Fig. 2L and fig. S4). For reference, TiO_2 nanoparticles, as well as isolated Ru atoms–decorated TiO_2 nanoparticles (TiO_2@Ru), have also been synthesized (figs. S1, E and F, and S2, G to I).
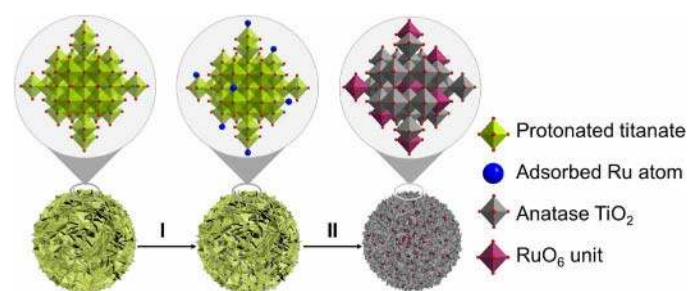

Fig. 1. Schematic illustration of the synthetic procedure of ME-TiO_2@Ru. Step I: Loading of the Ru component onto the surface of ME-PT. Step II: Pyrolysis of the Ru-loaded ME-PT for obtaining the final hybrid.

Extended XAFS (EXAFS) analyses at Ru K-edge are conducted to figure out the local coordination environment of the Ru species. The EXAFS spectra confirm that there is no Ru—Ru/Ru—O—Ru bonding in ME-TiO_2@Ru and TiO_2@Ru, thus ruling out the existence of Ru/RuO_2 particles or clusters (Fig. 3A) (*15*). The strong peaks at 1.49 Å indicate the presence of Ru—O bonds, confirming that the Ru atoms are isolated and coordinated with surrounding O atoms from TiO_2. The coordination sphere of the atomically dispersed centers is further quantified by least-squares EXAFS curve-fitting analyses (Fig. 3, B and C, and fig. S5). The best-fitted results confirm the Ru—O bond lengths of ME-TiO_2@Ru and TiO_2@Ru as 1.98 and 1.99 Å, respectively. These values are comparable to the Ru—O bonding (1.97 Å) in RuO_2 (table S1). Further quantitative EXAFS curve-fitting analyses confirm that the coordination numbers of the Ru—O bonding in the first coordination sphere are estimated to be 5.9 and 6.0 for ME-TiO_2@Ru and TiO_2@Ru, respectively. These results suggest that the decorated Ru sites keep the nearly identical configuration to that of Ti atoms in TiO_2. Wavelet transform (WT) simulations have also been conducted for interpreting a radial distance resolution in the *K* space. The WT intensity maximum near 5.8 Å^{-1} arising from the Ru—O coordination is well resolved at 1.0 to 3.0 Å for ME-TiO_2@Ru and TiO_2@Ru, whereas an intensity maximum at about 9.2 Å^{-1} associated with the Ru—Ru coordination is not observed (Fig. 3E and fig. S5C). These results further illustrate that the Ru species in ME-TiO_2@Ru and TiO_2@Ru are atomically dispersed without aggregation. For identifying the three-dimensional arrangement of atoms at higher sensitivity, x-ray absorption near-edge structure (XANES) analysis is applied (Fig. 3D). The notable difference of XANES profiles between ME-TiO_2@Ru

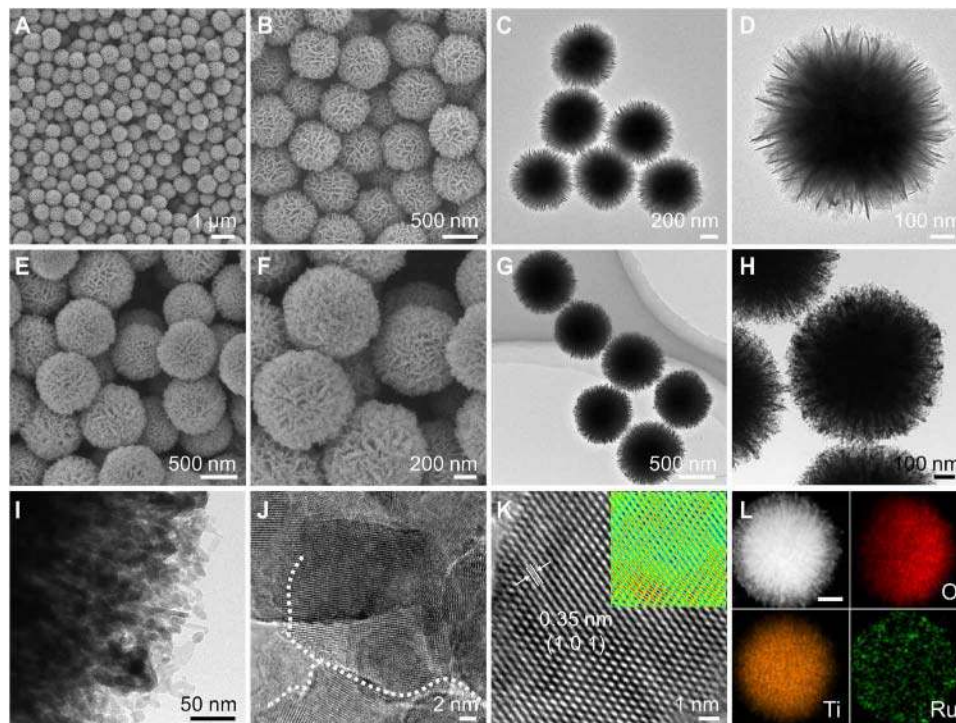**Fig. 2. Morphological, structural, and elemental characterizations.** (**A** and **B**) FESEM images of Ru-loaded ME-PT. (**C** and **D**) TEM images of Ru-loaded ME-PT. (**E** and **F**) FESEM images of ME-TiO_2@Ru. (**G** to **I**) TEM images of ME-TiO_2@Ru. (**J** and **K**) HRTEM images of ME-TiO_2@Ru. (**L**) HAADF-STEM image and related elemental mapping images of ME-TiO_2@Ru; scale bar, 200 nm.
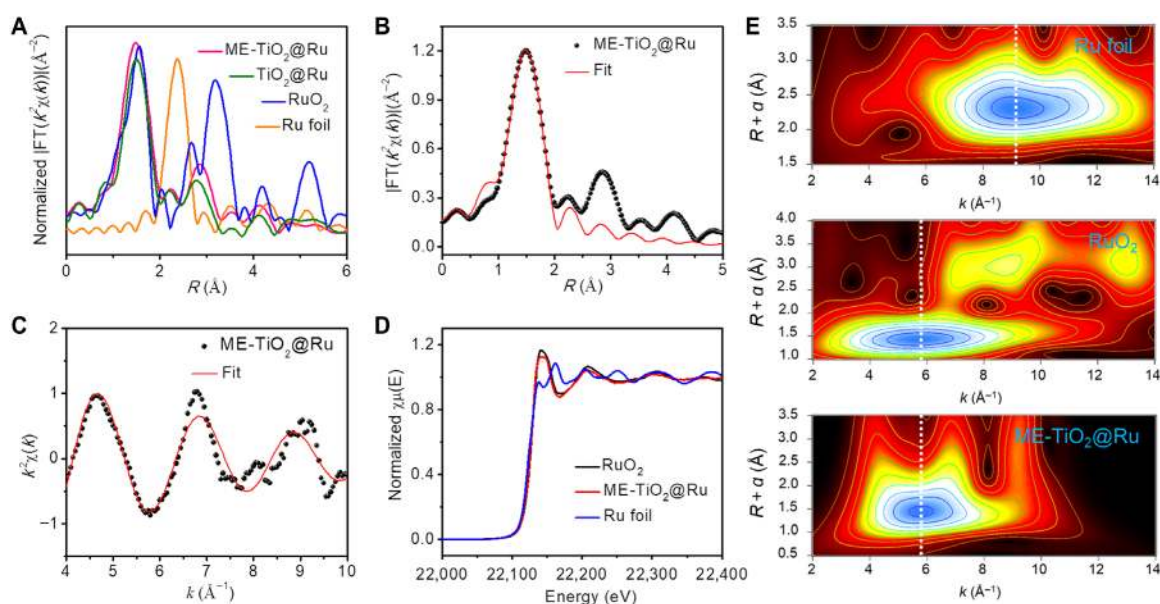
Fig. 3. EXAFS characterization. (**A**) Fourier-transformed magnitudes of the experimental Ru K-edge EXAFS spectra. (**B** and **C**) Fourier-transformed magnitudes of Ru K-edge EXAFS spectra in R space (B) and K space (C) for ME-TiO$_2$@Ru. (**D**) Ru K-edge XANES experimental spectra. (**E**) WT for the k^2-weighted EXAFS signal.

and Ru foil clearly excludes the Ru—Ru interaction in the as-prepared ME-TiO$_2$@Ru. With respect to the commercial RuO$_2$, the slightly reduced white-line intensity suggests that the oxidation state of Ru species in ME-TiO$_2$@Ru should be lower than tetravalence, demonstrating effective electronic coupling via the Ru—O bonding (16).

X-ray photoelectron spectroscopy (XPS) has also been applied to further provide the structural information. The high-resolution XPS spectrum for O 1s reveals the existence of Ti—O and Ti—O—Ti bonds in ME-TiO$_2$ with the binding energy peaks at 528.9 and 529.6 eV, respectively (fig. S6A). Ru—O and Ru—O—Ti bonds are also observed after the decoration of Ru species in ME-TiO$_2$@Ru (fig. S6B). It is worth noting that the binding energy of Ti 2p in ME-TiO$_2$@Ru increases about 0.6 eV when compared with that of ME-TiO$_2$, implying the intrinsic charge transfer between the Ru and TiO$_2$ (fig. S6C) (17). Raman modes at about 396, 514, and 635 cm^{-1} can be ascribed to the anatase phase of TiO$_2$ (fig. S6D). Lower intensity and larger width of these modes may indicate partial disorder and amorphization of TiO$_2$ in the ME-TiO$_2$@Ru (18). The relatively high porosity of ME-TiO$_2$@Ru has been confirmed by N$_2$ sorption isotherm measurement (fig. S6E). A typical type IV isotherm verifies the existence of micropores and mesopores in the hybrid (fig. S6F).

Evaluation of photocatalytic performance
Photocatalytic H$_2$ evolution performances are evaluated in a closed gas circulation system. By introducing a small amount of Ru (denoted as ME-TiO$_2$@Ru-0.36), the H$_2$ evolution rate of 187.2 μmol hour^{-1} is achieved, which is nearly 20 times higher than that of pure ME-TiO$_2$ (9.4 μmol hour^{-1}) (Fig. 4A). The above ME-TiO$_2$@Ru sample represents the optimized photocatalyst [Ru loading amount of 0.93 weight % (wt %)] with the highest H$_2$ evolution rate of 323.2 μmol hour^{-1}. This value is 34 times higher than that of pure ME-TiO$_2$. Further increasing the loading amount of Ru gives rise to slightly depressed activity. It is worth noting that the achieved H$_2$ evolution rate of the ME-TiO$_2$@Ru is much higher than that of Pt-based cocatalytic systems and among the highest reported values (table S2) (19). Time-dependent

H$_2$ evolutions demonstrate that the amount of generated H$_2$ increases almost linearly with the irradiation time (Fig. 4B). Compared with TiO$_2$@Ru with identical amount of Ru loading, ME-TiO$_2$@Ru exhibits a greatly boosted H$_2$ generation rate, which is 2.2 times higher than that of TiO$_2$@Ru. The turnover numbers (TONs) with respect to Ru atoms have also been calculated and confirmed as 384 and 175 for ME-TiO$_2$@Ru and TiO$_2$@Ru in 5 hours, respectively (20, 21). The wavelength-dependent H$_2$ evolution over the ME-TiO$_2$@Ru sample has also been investigated. The photocatalytic activity of ME-TiO$_2$@Ru agrees generally well with its characteristic absorption, which indicates that the H$_2$ production is driven by the photoexcitation (fig. S7, A and B) (22). The photocatalytic stability of the photocatalyst has also been evaluated with no obvious deactivation in H$_2$ evolution rate in five cycles (Fig. 4C).

DISCUSSION
To further elucidate the dynamic changes in the oxidation state and local coordination environment, in situ XAFS spectra are monitored during the photocatalytic H$_2$ evolution process. Figure 4D shows that the white-line peak of the as-prepared ME-TiO$_2$@Ru is centered at 22,144 eV. Upon light irradiation, the white-line intensity decreases obviously with the decrease of d band vacancy of Ru atoms, indicating that the Ru species is quickly reduced after receiving electrons from photo-excited TiO$_2$. The spectrum can nearly be restored to its initial state with the removal of the light source. The in situ quantitative EXAFS curve fitting further confirms the gradual configuration transformation of Ru species in the photocatalytic process (Fig. 4, E and F). A contracted Ru—O bond length (1.98 Å for light-off and 1.93 Å for light-on) and a reduced coordination number (from 5.9 to 4.6) have been observed after receiving the photogenerated electrons from TiO$_2$ in the excitation process, which confirm the variation of local electronic and structural properties of ME-TiO$_2$@Ru in the photocatalytic process. The newly generated configuration and reduced oxidation state are favorable for the
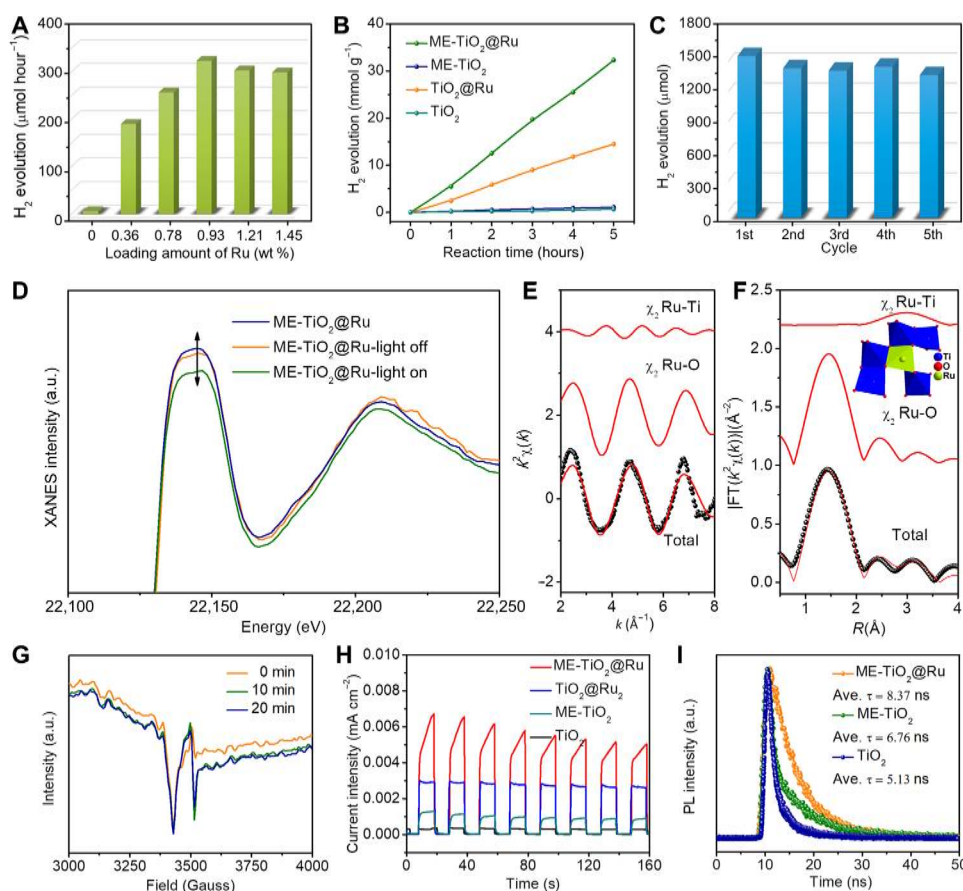
Fig. 4. H₂ evolution and operando x-ray absorption spectroscopy. (**A**) Photocatalytic H₂ generation rates of ME-TiO₂@Ru with different Ru loading amounts. (**B**) Time-dependent hydrogen evolution over different catalysts. (**C**) Recycling tests (5 hours per cycle) of photocatalytic H₂ generation of ME-TiO₂@Ru. (**D**) Normalized operando Ru K-edge XANES spectra for ME-TiO₂@Ru at various biases. (**E** and **F**) Ru K-edge EXAFS analysis of ME-TiO₂@Ru in K (E) and R (F) spaces, respectively. The inset shows the structure of ME-TiO₂@Ru under the reaction process. (**G**) Electron paramagnetic resonance spectra of ME-TiO₂@Ru after different irradiation times. (**H**) Transient photocurrent spectra. (**I**) Time-resolved photoluminescence spectra. a.u., arbitrary units.

bonding with water molecules, thus accelerating the water splitting (*23*). The change in the oxidation state is further elucidated by the electron paramagnetic resonance (EPR) investigation during the photo-excitation process (Fig. 4G). The proportionality factor (*g* factor) can be obtained from the EPR spectra, which is the unique property of the electron in a certain environment. The EPR spectrum of the initial sample exhibits the characteristic signal of hole-trapped O⁻ and electron-trapped Ti³⁺ (*24*). The photo-excitation produces two distinct changes in the EPR spectra in the excitation process. The characteristic Ru³⁺ (*g* = 2.002) is generated, accompanied by the production of more hole-trapped O⁻ (*25*). No further increase of Ru³⁺ is observed with the prolonging of the reaction time from 10 to 20 min, verifying the consumption of photogenerated electrons in the reaction.

The above results clearly demonstrate the reversible evolution of the active centers in the photocatalytic process. The catalytic activity is correlated with the separation efficiency of photo-excited electron-hole pairs and the migration rate to the active sites. To understand the origin of the enhancing effect, transient photocurrent responses are collected to study their charge generation and migration capabilities (Fig. 4H). The photocurrent density of ME-TiO₂@Ru is much higher than that of TiO₂@Ru and bare ME-TiO₂. These results not only confirm the positive effects of sharp boundaries in the

separation of photogenerated electron-hole pairs but also suggest that the isolated Ru atoms over ME-TiO₂ serve as "electron pumps" and promote the charge transfer and separation efficiency. This hypothesis is further supported by the electrochemical impedance spectroscopy measurements in 0.5 M Na₂SO₄ aqueous solution (fig. S7C). As observed, the ME-TiO₂@Ru exhibits a much lower charge-transfer resistance than TiO₂@Ru and bare ME-TiO₂. In addition, photoluminescence (PL) quenching measurements are also conducted to investigate the electron transfer process. Obvious PL quenching is observed after the decoration of isolated Ru atoms (fig. S7D). This result shows that the recombination of electron-hole pairs is effectively suppressed by the deposited cocatalyst. Time-resolved PL (TRPL) spectroscopy is used to probe the charge carrier dynamics of the materials (Fig. 4I). The decay kinetics of ME-TiO₂@Ru exhibits a longer average lifetime (8.37 ns) than that of TiO₂@Ru (6.76 ns) and ME-TiO₂ (5.13 ns), demonstrating that the ME-TiO₂@Ru can effectively promote the separation of photoinduced electrons and holes.

To gain further understanding of the efficiency of photo-excited charge carrier separation over atomic Ru-decorated TiO₂, we carry out some theoretical calculations based on density-functional theory (DFT) (fig. S8). Figure 5A shows the band structure of pure TiO₂. With the decoration of isolated Ru atoms, newly generated bands

appear in the vicinity of the Fermi level (Fig. 5B). These newly generated energy levels and the corresponding Kohn-Sham $4d$ orbitals of the Ru atoms are responsible for hydrogen adsorption (26). The adsorption free energy (E_0) of hydrogen is also investigated (fig. S9A). The calculated E_0 for pure TiO_2 is confirmed as 0.143 eV, revealing that hydrogen is not bound favorably to the undecorated surface (27). The hydrogen adsorption over ME-TiO_2 is a spontaneous process, evidenced by the E_0 value of −1.087 eV. With the surface decoration of Ru atoms, the hydrogen adsorptions are more favorably supported, which is essential for high catalytic performance. In addition, the inclusion of Ru atoms in TiO_2 makes remarkable contributions to the conduction band minimums, indicating that the Ru decoration can act as a mediator to promote the electron transfer.

Compared with the pure TiO_2, an increased total density of states (TDOS) is observed at the valence band maximum after Ru decoration, leading to an easier excitation and transfer of photogenerated electrons from TiO_2 to Ru centers (Fig. 5, C and D) (28). These occupied states of Ru largely turn into "electron trap" for TiO_2 and lift the Fermi level to the position close to the conduction band minimum of TiO_2. The unoccupied Ru states are located at the conduction band minimum of TiO_2 and have a low contribu-

tion to the TDOS. As observed from the calculated projected density of states (PDOS) of Ru atoms, the TiO_2@Ru and ME-TiO_2@Ru show frail Ru states with small intervals and bandgaps of 1.12 and 0.79 eV, respectively (Fig. 5, D and E, and fig. S9, B and C). These results demonstrate the strong electronic coupling between the isolated Ru atoms and the support and also verify that the decoration of Ru can accelerate the electron transfer with a narrower bandgap. In comparison to the Ru@TiO_2, ME-TiO_2@Ru could reduce the bandgap to a greater extent and result in more marked enhancement for the photogenerated charge separation. The differential electron densities clearly illustrate that the electrons tend to accumulate around the top valence band of TiO_2 slab after Ru decoration (Fig. 5, F and G) (29). These abundant localized electrons are expected to be transferred into the antibonding orbitals of water molecules for water activation. For ME-TiO_2@Ru, the valence band is primarily composed of the O atoms from the edges of TiO_2, while the conduction band mainly originates from Ru atoms (Fig. 5H) (22). It suggests that it is favorable for the photogenerated electrons to migrate from the edges of TiO_2 to the isolated Ru centers.

In summary, isolated Ru centers are successfully decorated onto the surface of the multi-edged TiO_2 spheres (ME-TiO_2@Ru) and applied as a catalyst for photocatalytic water-splitting. Remarkably,
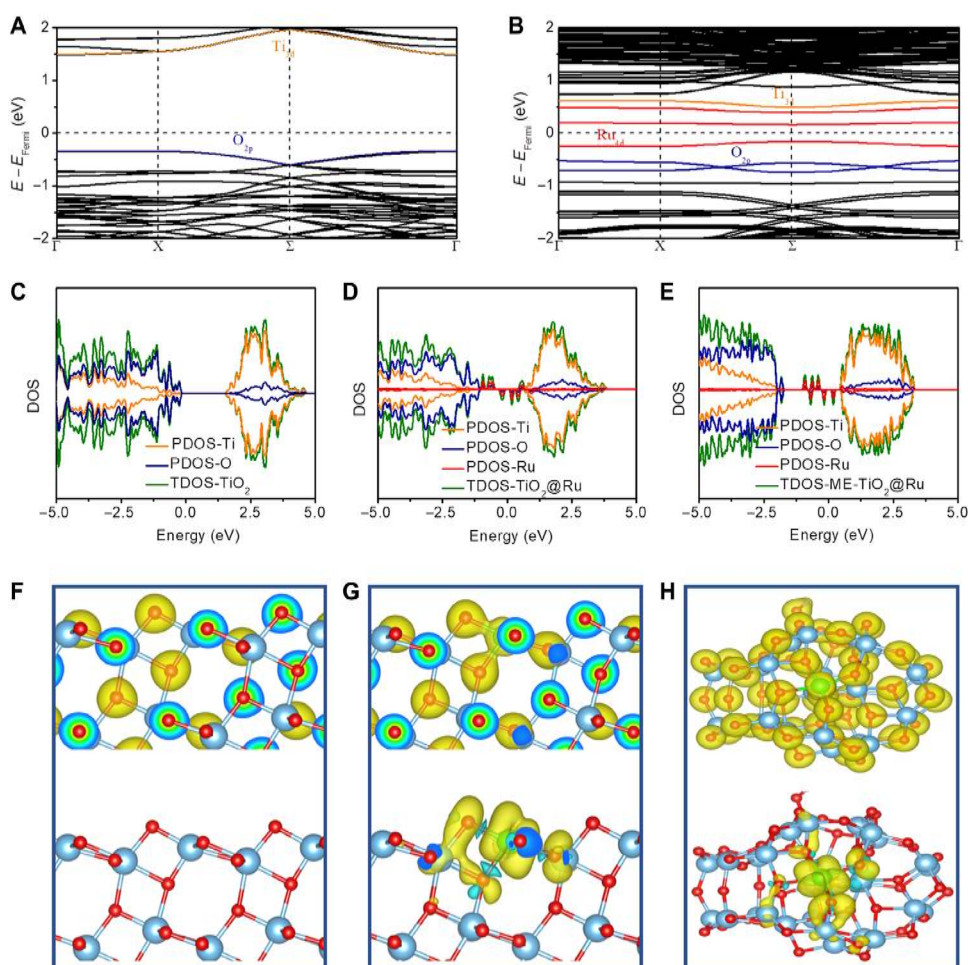

Fig. 5. DFT calculation. (**A** and **B**) Band structures of TiO_2 (A) and Ru-decorated TiO_2 (B). (**C** to **E**) Calculated density of states of TiO_2 (C), TiO_2@Ru (D), and ME-TiO_2@Ru (E). (**F** to **H**) Calculated distribution of charge density (top) and differential charge density (bottom) for TiO_2 (F), TiO_2@Ru (G), and ME-TiO_2@Ru (H).

the ME-TiO$_2$@Ru catalyst shows high photocatalytic activity and long-term catalytic stability. The unique atomic architecture of ME-TiO$_2$@Ru allows us to explore the origin of the high photocatalytic activity. As demonstrated by the energy transfer investigation and the first-principle calculation, the sharp edges of TiO$_2$ are favorable for transferring photogenerated electrons to the isolated Ru reactive centers. After receiving the photogenerated electrons, the Ru centers undergo reversible valence and configuration transformation. Our findings may provide new opportunities to design highly efficient photocatalysts for water splitting at atomic scale and advance our understanding of the hydrogen evolution process.

MATERIALS AND METHODS

Synthesis of ME-PT hierarchical spheres and Ru-loaded ME-PT hierarchical spheres

The ME-PT hierarchical spheres were synthesized by a facile solvothermal method. In a typical synthesis, 10 ml of N,N′-dimethylformamide and 30 ml of isopropyl alcohol were mixed as the organic solvent. After that, 1 ml of tetrabutyl orthotitanate (TBT) was added to the mixed organic solvent. The mixed solution was then transferred to a 60-ml Teflon-lined autoclave and heated in an electric oven at 200°C for 20 hours. Last, the product of ME-PT was centrifuged, washed thoroughly with ethanol, dried at 60°C overnight, and collected in 53% yield based on the TBT. The as-prepared ME-PT hierarchical spheres (100 mg) were mixed with a certain amount of RuCl$_3$ (1 mg for ME-TiO$_2$@Ru-0.36, 3 mg for ME-TiO$_2$@Ru-0.78, 5 mg for ME-TiO$_2$@Ru-0.93, 7 mg for ME-TiO$_2$@Ru-1.21, and 10 mg for ME-TiO$_2$@Ru-1.45) in ethanol solution (20 ml) for 2 hours, in which Ru species was loaded homogeneously on the surface of ME-PT hierarchical spheres with weak coordination, and then the sample was centrifuged and collected.

Synthesis of multi-edged TiO$_2$ (ME-TiO$_2$) hierarchical spheres and Ru species dispersed ME-TiO$_2$ (ME-TiO$_2$@Ru)

The ME-TiO$_2$ hierarchical spheres were obtained by controlled calcination of as-synthesized ME-PT hierarchical spheres at 450°C for 2 hours under air atmosphere. The loading of Ru on ME-TiO$_2$ is the same as the preparation of Ru-loaded ME-PT hierarchical spheres except the precursor was changed to ME-TiO$_2$.

Synthesis of TiO$_2$ nanoparticles and Ru species dispersed TiO$_2$ nanoparticles (TiO$_2$@Ru)

In a typical synthesis of TiO$_2$ nanoparticles, 1 ml of isopropyl titanate was mixed with 10 ml of ethanol solution and reacted for 1 hour. The obtained product was collected by centrifugation, washing, and drying, and then was calcined at 450°C for 2 hours under air atmosphere. The final yield is about 68% based on the isopropyl titanate precursor. TiO$_2$@Ru can be obtained by a similar method except that the precursor has to react with RuCl$_3$ in ethanol solution before calcination.

Characterizations

XRD patterns were characterized by XRD with graphite monochromatized Cu-Kα radiation (Bruker, D2 Phaser). Ultraviolet-visible (UV-vis) absorption was characterized by UV-vis spectroscopy (Shimadzu, UV-2450). PL spectra were acquired on Edinburgh Analytical Instruments FL/FSTCSPC980 coupled with a time-correlated single–photo-counting system at room temperature. For the measurement of PL lifetime, the used excitation wavelength (λ_{ex}) was 350 nm and the maximum emission wavelength (λ_{em}) was 550 nm. The average lifetime (Ave. τ) is calculated according to τ = τ$_1$·I$_1$ + τ$_2$·I$_2$ + τ$_3$·I$_3$ (τ$_i$ is the lifetime; I$_i$ is the relative intensity). Morphology and structure of the samples were characterized by FESEM (JEOL, JSM-6700F) and TEM (JEOL, JEM-2010). Zeta potentials were measured by laser particle size and zeta potential analyzer (Brookhaven, BI-200SM). Specifically, 5 mg of sample was dispersed in ethanol solution under ultrasonic treatment for 3 min before the zeta potential measurement. Surface chemical analysis was performed by XPS (ULVAC-PHI Inc., PHI Quantera SXM). Compositions of the samples were characterized by inductively coupled plasma optical emission spectrometry (Thermo Fisher Scientific, IRIS Intrepid II XSP spectrometer). Gas adsorption investigation was performed in the ASAP (Accelerated Surface Area and Porosimetry) 2020 System. EPR measurements were performed at room temperature on a Bruker E500 electron spin resonance spectrometer operating at about 9.0 GHz. The magnetic field was calibrated with Mn^{2+} in MgO.

Photocatalytic measurements

Photocatalytic performance was evaluated in a gas-closed circulation system equipped with a 300-W Xe lamp as the light source. Fifty milligrams of the sample was dispersed in 120 ml of methanol aqueous solution for the reaction. During the photocatalytic process, the reaction system was vigorously stirred by a magnetic stirrer, and the reaction temperature was controlled by circulating cooling water. TON is the number of generated moles of H$_2$ that a mole of cocatalyst can convert in 5 hours. The H$_2$ evolution was analyzed by an online gas chromatograph (GC-8A, Shimadzu Corp.) equipped with a thermal conductivity detector.

Collection, analysis, and modeling of x-ray absorption data

EXAFS refers to the oscillatory region of an x-ray absorption spectrum beginning about 30 eV above an absorption edge. Related data were collected at the beamline 1W1B of the Beijing Synchrotron Radiation Facility (BSRF, Beijing) in a fluorescence mode at room temperature. A Si (111) double-crystal monochromator was used to monochromatize the x-ray white beam. The typical energy of the storage ring was 2.5 GeV. Ru foil was used for calibration. Least-squares curve fitting analysis of the EXAFS data was performed using the Artemis program. The fittings were performed in both R space (R is the interatomic distance from the absorber atom) and K space (k is the wave vector) with application of k^0, k^1, and k^3 weightings. All fits were carried out with a k weight of 2. The EXAFS R factor (R_f), which measures the percentage misfit of the theory to the data, was used to evaluate the goodness of the fit. By providing not only radial distance resolution but also K space resolution, WT analysis is powerful for discriminating the backscattering atoms even when they overlap substantially in R space. The WT correlates the backscattering amplitudes of individual paths in K space and their interatomic distances in R space. A homemade photochemical setup equipped with a 300-W Xe lamp was used for in situ XAFS measurements. To guarantee the quality of the acquired data, a solid-state detector was also equipped in the in situ measurement. The acquired EXAFS data for in situ investigation were processed according to standard procedures using the ATHENA module implemented in the IFEFFIT software package (30). The EXAFS spectra were obtained by subtracting the post-edge background from

the overall absorption and then normalizing with respect to the edge-jump step.

Electrochemical measurements

The working electrode was fluorine-doped tin oxide glass deposited by TiO_2, ME-TiO_2, TiO_2@Ru, and ME-TiO_2@Ru (with an area of 0.25 cm^2 and 5 mg of samples in 500 μl of ethanol). The transient photocurrent responses were carried out in the same cell in 0.5 M Na_2SO_4 electrolyte using a bias potential at 0.25 V under on-off cycling irradiation by manual chopping.

Computational methods

All calculations were carried out with VASP (Vienna ab initio simulation package) code based on the DFT (22). The generalized gradient approximation was used for the exchange correlation energy. A plane-wave expansion for the basis set with a cutoff energy of 450 eV was used. To model the TCO and TiO_2 nanosheets, we constructed a slab model containing a Ru species covalently anchored on 4 × 4 supercells of the (101) TiO_2 surface with a vacuum region of 20 Å. For the surface termination of anatase TiO_2, Ti termination and O termination were considered in the proposed catalytic model. The anatase (101) surface was simulated with fully coordinated (Ti_{6c} and O_{3c}) and under-coordinated (Ti_{5c} and O_{2c}) atoms (fig. S8C) (31). We used 2 × 2 × 1 Monk-horst k-point meshes for the Brillouin-zone integrations of the slab model, respectively. All atoms were relaxed until the residual Hellmann-Feynman forces were less than that of 0.04 eV/Å. Moreover, the convergence for energy was chosen as 10^{-5} eV. No van der Waals interaction was considered in the simulation. For the models investigated in this work, the adsorption free energy (E_0) of the H^* was evaluated by the formula below

$$E_0 = \Delta E_{DFT} + \Delta ZPE - T\Delta S$$

where ΔE_{DFT}, ZPE, and S are the adsorption energy, zero-point energy, and entropy of the adsorbates, respectively.

SUPPLEMENTARY MATERIALS

Supplementary material for this article is available at http://advances.sciencemag.org/cgi/content/full/6/39/eabb9823/DC1

REFERENCES AND NOTES

1. J. Liu, Y. Liu, N. Liu, Y. Han, X. Zhang, H. Huang, Y. Lifshitz, S.-T. Lee, J. Zhong, Z. Kang, Metal-free efficient photocatalyst for stable visible water splitting via a two-electron pathway. *Science* **347**, 970–974 (2015).
2. X. Li, J. Yu, M. Jaroniec, Hierarchical photocatalysts. *Chem. Soc. Rev.* **45**, 2603–2636 (2016).
3. W.-J. Ong, L.-L. Tan, Y. H. Ng, S.-T. Yong, S.-P. Chai, Graphitic carbon nitride (g-C_3N_4)-based photocatalysts for artificial photosynthesis and environmental remediation: Are we a step closer to achieving sustainability? *Chem. Rev.* **116**, 7159–7329 (2016).
4. H. Duan, J.-C. Liu, M. Xu, Y. Zhao, X.-L. Ma, J. Dong, X. Zheng, J. Zheng, C. S. Allen, M. Danaie, Y.-K. Peng, T. Issariyakul, D. Chen, A. I. Kirkland, J.-C. Buffet, J. Li, S. C. E. Tsang, D. O'Hare, Molecular nitrogen promotes catalytic hydrodeoxygenation. *Nat. Catal.* **2**, 1078–1087 (2019).
5. S. Wang, B. Y. Guan, X. Wang, X. W. Lou, Formation of hierarchical Co_9S_8@$ZnIn_2S_4$ heterostructured cages as an efficient photocatalyst for hydrogen evolution. *J. Am. Chem. Soc.* **140**, 15145–15148 (2018).
6. G. Xu, H. Zhang, J. Wei, H.-X. Zhang, X. Wu, Y. Li, C. Li, J. Zhang, J. Ye, Integrating the g-C_3N_4 nanosheet with B-H bonding decorated metal-organic framework for CO_2 activation and photoreduction. *ACS Nano* **12**, 5333–5340 (2018).
7. Q. Wang, T. Hisatomi, Q. Jia, H. Tokudome, M. Zhong, C. Wang, Z. Pan, T. Takata, M. Nakabayashi, N. Shibata, Y. Li, I. D. Sharp, A. Kudo, T. Yamada, K. Domen, Scalable water splitting on particulate photocatalyst sheets with a solar-to-hydrogen energy conversion efficiency exceeding 1%. *Nat. Mater.* **15**, 611–615 (2016).
8. H. Zhang, W. Zhou, X. F. Lu, T. Chen, X. W. Lou, Implanting isolated Ru atoms into edge-rich carbon matrix for efficient electrocatalytic hydrogen evolution. *Adv. Energy Mater.* **10**, 2000882 (2020).
9. A. Wang, J. Li, T. Zhang, Heterogeneous single-atom catalysis. *Nat. Rev. Chem.* **2**, 65–81 (2018).
10. X. Li, Y. Huang, B. Liu, Catalyst: Single-atom catalysis: Directing the way toward the nature of catalysis. *Chem* **5**, 2733–2735 (2019).
11. H. Zhang, G. Liu, L. Shi, H. Liu, T. Wang, J. Ye, Engineering coordination polymers for photocatalysis. *Nano Energy* **22**, 149–168 (2016).
12. L. Huang, J. Chen, L. Gan, J. Wang, S. Dong, Single-atom nanozymes. *Sci. Adv.* **5**, eaav5490 (2019).
13. H. B. Wu, X. W. Lou, H. H. Hng, Synthesis of uniform layered protonated titanate hierarchical spheres and their transformation to anatase TiO_2 for lithium-ion batteries. *Chem. Eur. J.* **18**, 2094–2099 (2012).
14. J. B. Park, J. Graciani, J. Evans, D. Stacchiola, S. Ma, P. Liu, A. Nambu, J. F. Sanz, J. Hrbek, J. A. Rodriguez, High catalytic activity of Au/CeO_x/TiO_2 (110) controlled by the nature of the mixed-metal oxide at the nanometer level. *Proc. Natl. Acad. Sci. U.S.A.* **106**, 4975–4980 (2009).
15. X.-F. Yang, A. Wang, B. Qiao, J. Li, J. Liu, T. Zhang, Single-atom catalysts: A new frontier in heterogeneous catalysis. *Acc. Chem. Res.* **46**, 1740–1748 (2013).
16. H. Zhang, W. Zhou, T. Chen, B. Y. Guan, Z. Li, X. W. Lou, A modular strategy for decorating isolated cobalt atoms into multichannel carbon matrix for electrocatalytic oxygen reduction. *Energy Environ. Sci.* **11**, 1980–1984 (2018).
17. T. Zheng, K. Jiang, N. Ta, Y. Hu, J. Zeng, J. Liu, H. Wang, Large-scale and highly selective CO_2 electrocatalytic reduction on nickel single-atom catalyst. *Joule* **3**, 265–278 (2019).
18. J. Prakash, S. Sun, H. C. Swart, R. K. Gupta, Noble metals-TiO_2 nanocomposites: From fundamental mechanisms to photocatalysis, surface enhanced Raman scattering and antibacterial applications. *Appl. Mater. Today* **11**, 82–135 (2018).
19. G. Liu, G. Zhao, W. Zhou, Y. Liu, H. Pang, H. Zhang, D. Hao, X. Meng, P. Li, T. Kako, J. Ye, In situ bond modulation of graphitic carbon nitride to construct p–n homojunctions for enhanced photocatalytic hydrogen production. *Adv. Funct. Mater.* **26**, 6822–6829 (2016).
20. J. Cai, J. Shen, X. Zhang, Y. H. Ng, J. Huang, W. Guo, C. Lin, Y. Lai, Light-driven sustainable hydrogen production utilizing TiO_2 nanostructures: A review. *Small Methods* **3**, 1800184 (2019).
21. B.-H. Lee, S. Park, M. Kim, A. K. Sinha, S. C. Lee, E. Jung, W. J. Chang, K.-S. Lee, J. H. Kim, S.-P. Cho, H. Kim, K. T. Nam, T. Hyeon, Reversible and cooperative photoactivation of single-atom Cu/TiO_2 photocatalysts. *Nat. Mater.* **18**, 620–626 (2019).
22. H. Zhang, P. Zhang, M. Qiu, J. Dong, Y. Zhang, X. W. Lou, Ultrasmall MoO_x clusters as a novel cocatalyst for photocatalytic hydrogen evolution. *Adv. Mater.* **31**, 1804883 (2019).
23. S. Zhao, Y. Wang, J. Dong, C.-T. He, H. Yin, P. An, K. Zhao, X. Zhang, C. Gao, L. Zhang, J. Lv, J. Wang, J. Zhang, A. M. Khattak, N. A. Khan, Z. Wei, J. Zhang, S. Liu, H. Zhao, Z. Tang, Ultrathin metal-organic framework nanosheets for electrocatalytic oxygen evolution. *Nat. Energy* **1**, 16184 (2016).
24. N. Siemer, A. Lüken, M. Zalibera, J. Frenzel, D. Muñoz-Santiburcio, A. Savitsky, W. Lubitz, M. Muhler, D. Marx, J. Strunk, Atomic-scale explanation of O_2 activation at the Au-TiO_2 interface. *J. Am. Chem. Soc.* **140**, 18082–18092 (2018).
25. R. Prabhakaran, V. Krishnan, A. Geetha, H. Bertagnolli, K. Natarajan, Synthesis, EPR, electrochemistry and EXAFS studies of ruthenium (III) complexes with a symmetrical tetradentate N_2O_2 schiff base. *Inorg. Chim. Acta* **359**, 1114–1120 (2006).
26. J. Zhang, Y. Zhao, X. Guo, C. Chen, C.-L. Dong, R.-S. Liu, C.-P. Han, Y. Li, Y. Gogotsi, G. Wang, Single platinum atoms immobilized on an MXene as an efficient catalyst for the hydrogen evolution reaction. *Nat. Catal.* **1**, 985–992 (2018).
27. S. Ida, N. Kim, E. Ertekin, S. Takenaka, T. Ishihara, Photocatalytic reaction centers in two-dimensional titanium oxide crystals. *J. Am. Chem. Soc.* **137**, 239–244 (2014).
28. Z. Geng, X. Kong, W. Chen, H. Su, Y. Liu, F. Cai, G. Wang, J. Zeng, Oxygen vacancies in ZnO nanosheets enhance CO_2 electrochemical reduction to CO. *Angew. Chem. Int. Ed.* **57**, 6054–6059 (2018).
29. J. Wang, L. Gan, W. Zhang, Y. Peng, H. Yu, Q. Yan, X. Xia, X. Wang, In situ formation of molecular Ni-Fe active sites on heteroatom-doped graphene as a heterogeneous electrocatalyst toward oxygen evolution. *Sci. Adv.* **4**, eaap7970 (2018).
30. B. Ravel, M. Newville, ATHENA, ARTEMIS, HEPHAESTUS: Data analysis for x-ray absorption spectroscopy using IFEFFIT. *J. Synchrotron Radiat.* **12**, 537–541 (2005).
31. H. G. Yang, C. H. Sun, S. Z. Qiao, J. Zou, G. Liu, S. C. Smith, H. M. Cheng, G. Q. Lu, Anatase TiO_2 single crystals with a large percentage of reactive facets. *Nature* **453**, 638–641 (2008).
32. S. Yang, Y. Gong, J. Zhang, L. Zhan, L. Ma, Z. Fang, R. Vajtai, X. Wang, P. M. Ajayan, Exfoliated graphitic carbon nitride nanosheets as efficient catalysts for hydrogen evolution under visible light. *Adv. Mater.* **25**, 2452–2456 (2013).

33. M.-Q. Yang, Y.-J. Xu, W. Lu, K. Zeng, H. Zhu, Q.-H. Xu, G. W. Ho, Self-surface charge exfoliation and electrostatically coordinated 2D hetero-layered hybrids. *Nat. Commun.* **8**, 14224 (2017).

34. H. Li, Y. Sun, Z.-Y. Yuan, Y.-P. Zhu, T.-Y. Ma, Titanium phosphonate based metal-organic frameworks with hierarchical porosity for enhanced photocatalytic hydrogen evolution. *Angew. Chem. Int. Ed.* **57**, 3222–3227 (2018).

35. J. Xie, S. A. Shevlin, Q. Ruan, S. J. A. Moniz, Y. Liu, X. L. Liu, Y. Li, C. C. Lau, Z. Guo, J. Tang, Efficient visible light–driven water oxidation and proton reduction by an ordered covalent triazine-based framework. *Energy Environ. Sci.* **11**, 1617–1624 (2018).

36. Y. Wang, X. Liu, J. Liu, B. Han, X. Hu, F. Yang, Z. Xu, Y. Li, S. Jia, Z. Li, Y. Zhao, Carbon quantum dot implanted graphite carbon nitride nanotubes: Excellent charge separation and enhanced photocatalytic hydrogen evolution. *Angew. Chem. Int. Ed.* **57**, 5765–5771 (2018).

37. S.-Y. Han, D.-L. Pan, H. Chen, X.-B. Bu, Y.-X. Gao, H. Gao, Y. Tian, G.-S. Li, G. Wang, S.-L. Cao, C.-Q. Wan, G.-C. Guo, A methylthio-functionalized-MOF photocatalyst with high performance for visible-light–driven H₂ evolution. *Angew. Chem. Int. Ed.* **57**, 9864–9869 (2018).

38. T. Banerjee, F. Haase, G. Savasci, K. Gottschling, C. Ochsenfeld, B. V. Lotsch, Single-site photocatalytic H₂ evolution from covalent organic frameworks with molecular cobaloxime co-catalysts. *J. Am. Chem. Soc.* **139**, 16228–16234 (2017).

39. Y. Zheng, L. Lin, X. Ye, F. Guo, X. Wang, Helical graphitic carbon nitrides with photocatalytic and optical activities. *Angew. Chem. Int. Ed.* **53**, 11926–11930 (2014).

40. N. Meng, J. Ren, Y. Liu, Y. Huang, T. Petit, B. Zhang, Engineering oxygen-containing and amino groups into two-dimensional atomically-thin porous polymeric carbon nitrogen for enhanced photocatalytic hydrogen production. *Energy Environ. Sci.* **11**, 566–571 (2018).